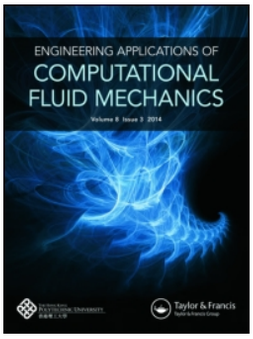

Engineering Applications of Computational Fluid Mechanics

ISSN: 1994-2060 (Print) 1997-003X (Online) Journal homepage: https://www.tandfonline.com/loi/tcfm20

Use of computational fluid dynamics to implement an aerodynamic inverse design method based on exact Riemann solution and moving wall boundary

Yu Duan, Qun Zheng & Bin Jiang

To cite this article: Yu Duan, Qun Zheng & Bin Jiang (2020) Use of computational fluid dynamics to implement an aerodynamic inverse design method based on exact Riemann solution and moving wall boundary, Engineering Applications of Computational Fluid Mechanics, 14:1, 284-298, DOI: 10.1080/19942060.2020.1711812

To link to this article: https://doi.org/10.1080/19942060.2020.1711812

© 2020 The Author(s). Published by Informa UK Limited, trading as Taylor & Francis Group

Published online: 12 Jan 2020.

Submit your article to this journal

View related articles

View Crossmark data

Full Terms & Conditions of access and use can be found at
https://www.tandfonline.com/action/journalInformation?journalCode=tcfm20

ENGINEERING APPLICATIONS OF COMPUTATIONAL FLUID MECHANICS
2020, VOL. 14, NO. 1, 284–298
https://doi.org/10.1080/19942060.2020.1711812

Taylor & Francis
Taylor & Francis Group

OPEN ACCESS Check for updates

Use of computational fluid dynamics to implement an aerodynamic inverse design method based on exact Riemann solution and moving wall boundary

Yu Duan, Qun Zheng and Bin Jiang

College of Power and Energy Engineering, Harbin Engineering University, Harbin, People's Republic of China

ABSTRACT
An aerodynamic inverse design method, which is used in compressors, is introduced in this paper. This inverse design method is based on the exact solution of the local Riemann problem on moving blade surfaces. Furthermore, an improved relaxation factor is added to control the induced velocity for reasonable deformation sizes in different cases. The viscous flow analysis and the inverse design are integrated in the computational fluid dynamics software ANSYS Fluent using the dynamic mesh user-defined function, which reduces the time spent on remeshing the computational domain. A compressor cascade is taken to illustrate the effect of this inverse design method. Using the compressor model, the case of a different loading pattern design under a high subsonic flow regime and the case of a loading smooth design under a transonic flow regime have proved the capability of this inverse design method to realize the prescribed pressure loading distribution.

ARTICLE HISTORY
Received 23 September 2019
Accepted 26 December 2019

KEYWORDS
CFD; aerodynamic design; turbomachinery; Riemann problem; moving wall boundary

Nomenclature

a	speed of sound
F	flux vector
k	specific heat ratio
p	static pressure
S	source term
u	velocity
W	conservative variable
y^+	y plus number
Γ	diffusion coefficient
Δ	blade displacement
Δp	pressure loading
θ	maximum thickness
ρ	density
φ	certain scalar
ω	relaxation factor

Subscripts

A	element A
g	at the mesh
d	prescribed parameter
L	left solution
max	maximum value
meanline	at the meanline
ps	pressure surface
R	right solution
ss	suction surface
V	virtual element
wall	at the wall
$*$	Riemann solution

Superscript

n	current time step

1. Introduction

Compressors are key aerodynamic components in aircraft engines. Their aerodynamic performance has crucial impacts on the running of aircraft engines. Aerodynamic design methods can be roughly classified into two types: one is the analysis design method used in traditional design systems; and the other is the inverse design method. In view of the excellent predictions obtained from computational fluid dynamics (CFD) in different simulations (Eivaz et al., 2018; Ghalandari, Mirzadeh Koohshahi, Mohamadian, Shamshirband, & Chau, 2019; Mosavi, Shamshirband, Salwana, Chau, & Tah, 2019), CFD is applied to check the aerodynamic intentions in the analysis design. There are always certain discrepancies between design targets and CFD; therefore, human modifications to blade geometries are inevitable. However, these artificial adjustments to blade geometries are not easy to make. This work requires that the designers

CONTACT Bin Jiang jiangbin_hrbeu@126.com

© 2020 The Author(s). Published by Informa UK Limited, trading as Taylor & Francis Group
This is an Open Access article distributed under the terms of the Creative Commons Attribution License (http://creativecommons.org/licenses/by/4.0/), which permits unrestricted use, distribution, and reproduction in any medium, provided the original work is properly cited.

are equipped with profound comprehension as well as insights into aerodynamics. The main disadvantages of the analysis design method are that inherent links between flow characteristics and blade geometry are implicit. Besides, human modifications to blade geometries depend strongly on individual experience. In general, a complete analysis design process needs many iterations to realize the design intentions. As a consequence, the analysis design method is fairly time consuming and costly.

The inverse design technique is able to overcome the aforementioned defects. One conspicuous advantage of inverse design is its ability to build direct links between the desired flow and blade geometries. In contrast to the analysis design, the static pressure or pressure loading along blade surfaces is prescribed as the boundary conditions in the inverse design. Starting from an initial-guess blade profile, the final convergence solution of inverse design is the desired blade geometry, which corresponds with the prescribed static pressure or pressure loading distribution on blade surfaces. Compared with the analysis design, the inverse design not only reduces manual interventions but also further decreases design difficulties. It is very economical in terms of resource consumption because explicit links are established between flow fields and blade geometries.

Many researchers have proposed inverse design methods. In the early days, Lighthill (1945), Sanz (1988) and Borges (1990) implemented inverse design algorithms based on analytical solutions of potential flow equations. In these inverse design methods, the flow was assumed to be incompressible and irrotational. Although inverse design solutions could be obtained quickly, these methods were difficult to extend to the actual three-dimensional flow owing to the assumption of potential flow. Despite this, their work provided a starting point for the research on inverse methods.

Dang and colleagues developed an inverse design method based on Euler equations (Dang & Isgro, 1995; Dang, Damle, & Qiu, 2000). In their method, the normal velocity, caused by the difference between current pressure and prescribed pressure on the blade surfaces, could exist during the inverse design process. The blade was updated using the 'tangency condition'. With the inverse design calculation approaching convergence, the normal velocity on blade surfaces would gradually decrease and finally vanish. This is totally different from the analysis computation. A similar inverse design method can be found in the work of Demeulenaere and Van den Braembussche (1998). In their method, the blade was updated using the transpiration model. It should be noted that the viscous effect was not considered in these methods. Thus, the inverse design solution is an 'inviscid geometry', in effect. Even though the viscous flow can be taken into account with certain techniques, it is impossible for this method to realize inverse design using an analysis solver without any modifications.

Inspired by the work of Thompkins and Tong (1982), Ghaly and co-workers proposed a novel inverse design method based on the virtual velocity or induced velocity (Roidl & Ghaly, 2010) and implemented the inverse design method using ANSYS CFX (Arbabi & Ghaly, 2013; Arbabi, Ghaly, & Medd, 2017). Madadi, Kermani, and Nili (2015) presented an inverse design method based on the ball–spine algorithm, and used it to improve the performance of an axial compressor. These inverse design methods are able to take the viscous effect into account. More important, they can be readily implemented using the flow solver with no modifications. However, extra time is needed to remesh the computational domain at each deformation step during the inverse design process, and the constant relaxation factor used to control the deformation size is strongly case dependent.

In this paper, the virtual velocity on the blade surfaces is defined using the exact solution of the local Riemann problem on moving blade surfaces with the 'no-slip' condition (Ferlauto & Marsilio, 2006; Mileshin, Orekhov, Shchipin, & Startsev, 2004). The normal thickness distribution is prescribed for preventing the blade intersection. The core of this inverse design method is realized by embedding a user-defined function (UDF) in ANSYS Fluent and executed in the transient calculation of the Navier–Stokes (N-S) solver with a dynamic mesh. In this way, the viscous effect is taken into account in the computation, and the application of the dynamic mesh saves the time spent on regenerating the mesh of the computational domain. The reason for choosing commercial software as the CFD solver is that abundant numerical algorithms and flow models are provided for selection. Furthermore, the robustness and accuracy of commercial CFD software have been verified by a significant number of numerical tests. A variable relaxation factor is also proposed to replace the constant relaxation factor used in previous studies for reasonable deformation sizes in different cases.

During the inverse design calculation process in all cases, the normal thickness distribution extracted from the original geometry is kept unchanged. The cubic polynomial fitting based on least squares is employed as the smooth method for ensuring reasonable blade profiles. Those geometric constraints are not only beneficial to improve calculation stability but also guarantee the manufacturability of the blade profiles obtained from the inverse design calculation.

Finally, a recovery test has been successfully carried out to validate the developed inverse design algorithm and two inverse design cases of the compressor cascade V103-220 demonstrate the decrease in total pressure loss

by reorganizing the pressure loading distribution on the blade surfaces.

2. Flow-governing equations and numerical methods

In the process of inverse design, the two-dimensional unsteady Reynolds-averaged Navier–Stokes (URANS) equations with dynamic mesh are taken to describe the flow field. For a certain scalar φ, the integral form of conservative equations can be written as follows:

$$\frac{d}{dt}\int \rho\varphi dV + \int \rho\varphi(\boldsymbol{u}-\boldsymbol{u_g})\cdot d\boldsymbol{A} = \int \Gamma\nabla\varphi\cdot d\boldsymbol{A} + \int S\varphi dV \tag{1}$$

where $\boldsymbol{u}$ is the flow velocity vector and $\boldsymbol{u_g}$ is the mesh velocity vector, ρ represents the density of gas, Γ is the diffusion coefficient, and S denotes the source term. For the time term, a first order implicit formula is used for time discretization. The finite volume method is used for space discretization. Specifically, a second order upwind scheme is applied to the convective term. The flow flux across the surface of the control volume is computed using the Roe–flux-difference splitting method, which is able to capture shock waves. In all cases in this paper, the Spalart–Allmaras (S-A) one-equation turbulence model is used to predict Reynolds stress for equation closure.

At the inlet of the computational domain, the boundary condition is specified as the pressure-inlet condition, which is specified by the total pressure, total temperature and direction of upstream flow. At the exit of the computational domain, the boundary condition is specified as the pressure-outlet condition, which is specified by the static pressure. The flow field is solved by simulating a single blade passage while imposing the periodic boundary condition on adjacent blade passages. The blade surfaces are specified as the moving wall boundary condition by introducing the inverse design UDF.

3. Inverse design method

3.1. Exact Riemann problem solution

The Riemann problem is a special problem in the hyperbolic partial differential equation with discontinuous initial values. The Riemann problem of one-dimensional unsteady Euler equations, which are quasi-linear hyperbolic systems, can be described in the following form:

$$\begin{cases} W_t + F_x = 0 \\ W(x,0) = \begin{cases} W_L & \text{if} \quad x<0 \\ W_R & \text{if} \quad x>0 \end{cases} \end{cases} \tag{2}$$

where W is the conservative variable, F is the flux vector, and W_L and W_R are the initial values of the conservative variable W.

The exact solution of the Riemann problem can be regarded as the combination of different elementary waves, including rarefaction waves, contact discontinuities and shock waves. There are four possible solutions to the Riemann problem, as shown in Figure 1.

For the case of left or right shock, there are relations between the primitive variables crossing a shock, according to Rankine–Hugoniot conditions:

$$\begin{aligned} u_L - u_{L*} &= (p_{L*}-p_L)\sqrt{\frac{2}{[(k+1)p_{L*}+(k-1)p_L]\rho_L}} \\ u_{R*} - u_R &= (p_{R*}-p_R)\sqrt{\frac{2}{[(k+1)p_{R*}+(k-1)p_R]\rho_R}} \end{aligned} \tag{3}$$

Generalized Riemann invariants are preserved when crossing a rarefaction wave. Hence, the formula of primitive variables across a rarefaction wave is given as

$$\begin{aligned} u_{L*} - u_L &= \frac{2a_L}{k-1}\left[\left(\frac{p_{L*}}{p_L}\right)^{\frac{k-1}{2k}} - 1\right] \\ u_{R*} - u_R &= \frac{2a_R}{k-1}\left[\left(\frac{p_{R*}}{p_R}\right)^{\frac{k-1}{2k}} - 1\right] \end{aligned} \tag{4}$$

3.2. Moving wall boundary condition

In Figure 2, a local Riemann problem is constructed on a moving wall at a speed of u_{wall}. Suppose that a virtual element V exists outside the fluid domain and is symmetrical with an element A positioned in the fluid domain. At the current time step n, the relation between primitive variables on element V and element A has the following assumption:

$$\begin{cases} \rho_A^n = \rho_V^n \\ u_A^n = -u_V^n + 2u_{\text{wall}} \\ p_A^n = p_V^n \end{cases} \tag{5}$$

According to formulae (3)–(5), the exact solution of the Riemann problem on the moving wall boundary can be concluded as

$$|u_* - u_A| = \begin{cases} (p_*-p_A)\sqrt{\frac{2}{[(k+1)p_*+(k-1)p_A]\rho_A}} & \text{if} \quad p_* > p_A \\ \frac{2a_A}{k-1}\left[1-\left(\frac{p_*}{p_A}\right)^{\frac{k-1}{2k}}\right] & \text{if} \quad p_* \le p_A \end{cases} \tag{6}$$

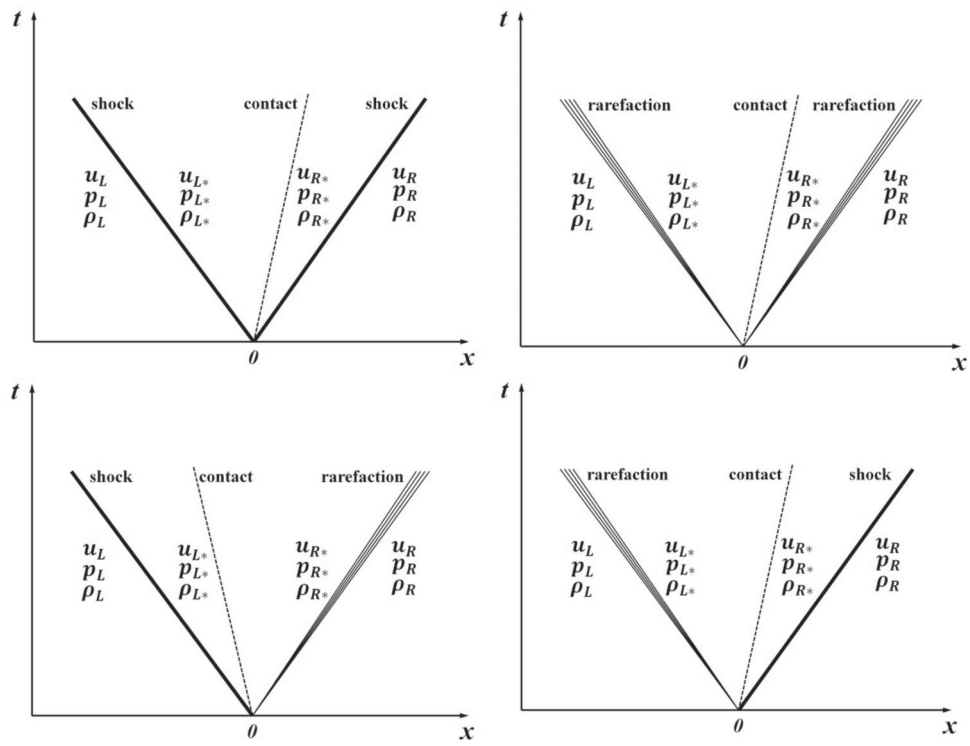

Figure 1. Exact solution of the Riemann problem.

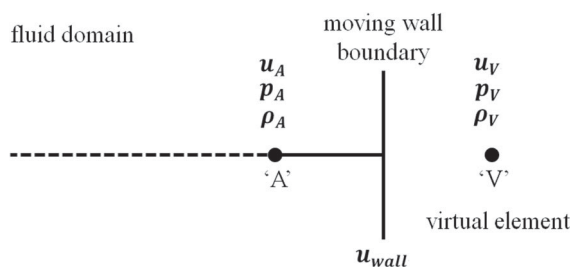

Figure 2. Schematic diagram of moving wall boundary conditions.

3.3. Inverse design method

When the inverse design approaches convergence, u_{wall} has to go to zero and p_* goes to the target pressure p_d gradually. As a result, u_{wall} is imposed as zero and p_* is enforced with the target static pressure p_d. At the current time step n, the expression of induced velocity u^n is derived from formula (6) and shown as

$$|u^n| = \begin{cases} (p_d - p^n)\sqrt{\frac{2}{[(k+1)p_d+(k-1)p^n]\rho^n}} & \text{if} \quad p_d > p^n \\ \dfrac{2a^n}{k-1}\left[1-\left(\dfrac{p_d}{p^n}\right)^{\frac{k-1}{2k}}\right] & \text{if} \quad p_d \le p^n \end{cases} \tag{7}$$

Imposing the 'no-slip' boundary condition to develop inverse design methods was also adopted by other researchers (Daneshkhah & Ghaly, 2007; Demeulenaere, Léonard, & Van den Braembussche, 1997; Van Rooij & Medd, 2012). Although they did not present a clear discussion on the ill-posedness issue, the robustness, flexibility and usefulness of this approach were demonstrated by different redesign cases. From their results, it seems that their inverse design methods were well posed.

It is also noted that the inverse design may become ill-posed when imposing the back-pressure for highly negative exit angles such as the turbine nozzle. The existence of more than one solution was theoretically demonstrated by Zannetti and Pandolfi (1984). It was suggested to give the outlet flow angle or the mass flow to avoid the ill-posedness. De Vito, Van den Braembussche, and Deconinck (2002) found that imposing the back-pressure seems to be well posed when designing for moderate negative exit angles (turbine rotor) and positive exit angles (compressor blades). In this paper, no ill-posed problem is met when implementing the compressor inverse design.

Sometimes, excessive deformations may induce intensive disturbance in the flow field and cause the failure of inverse design. Therefore, it is necessary to introduce a relaxation factor ω to control the induced velocity. In previous studies, the relaxation factor was generally set to be a constant. However, the drawback is that the appropriate value of ω is strongly case dependent and many numerical trials are needed to decide its value. Inspired by the

work of Yang, Liu, Wang, and Wu (2017), the definition of ω is given as

$$\omega = \left(\frac{u_{\max}}{(u_{\max})_{\max}}\right)^{\alpha} \frac{\beta \cdot \theta}{u_{\max}} \tag{8}$$

where $u_{\max}$ is the maximum value of induced velocity u^n on the blade wall, $(u_{\max})_{\max}$ is the maximum value of $u_{\max}$ during the inverse design process, and θ is the maximum normal thickness of the original blade. In most cases, default values of $\alpha = 2$ and $\beta = 0.1$ have fairly good effects on computational speed and stability. For some cases of extreme difficulty in convergence, parameters α and β could be adjusted to control the induced velocity.

The final expression of displacement on the blade surfaces is

$$\Delta = \omega \cdot u^n \tag{9}$$

In the inverse design, there are different choices for the design variables. In this paper, the pressure loading distribution Δp_d on the blade surface is regarded as a design variable. The axial chord length and normal thickness distribution of the original blade are kept unchanged

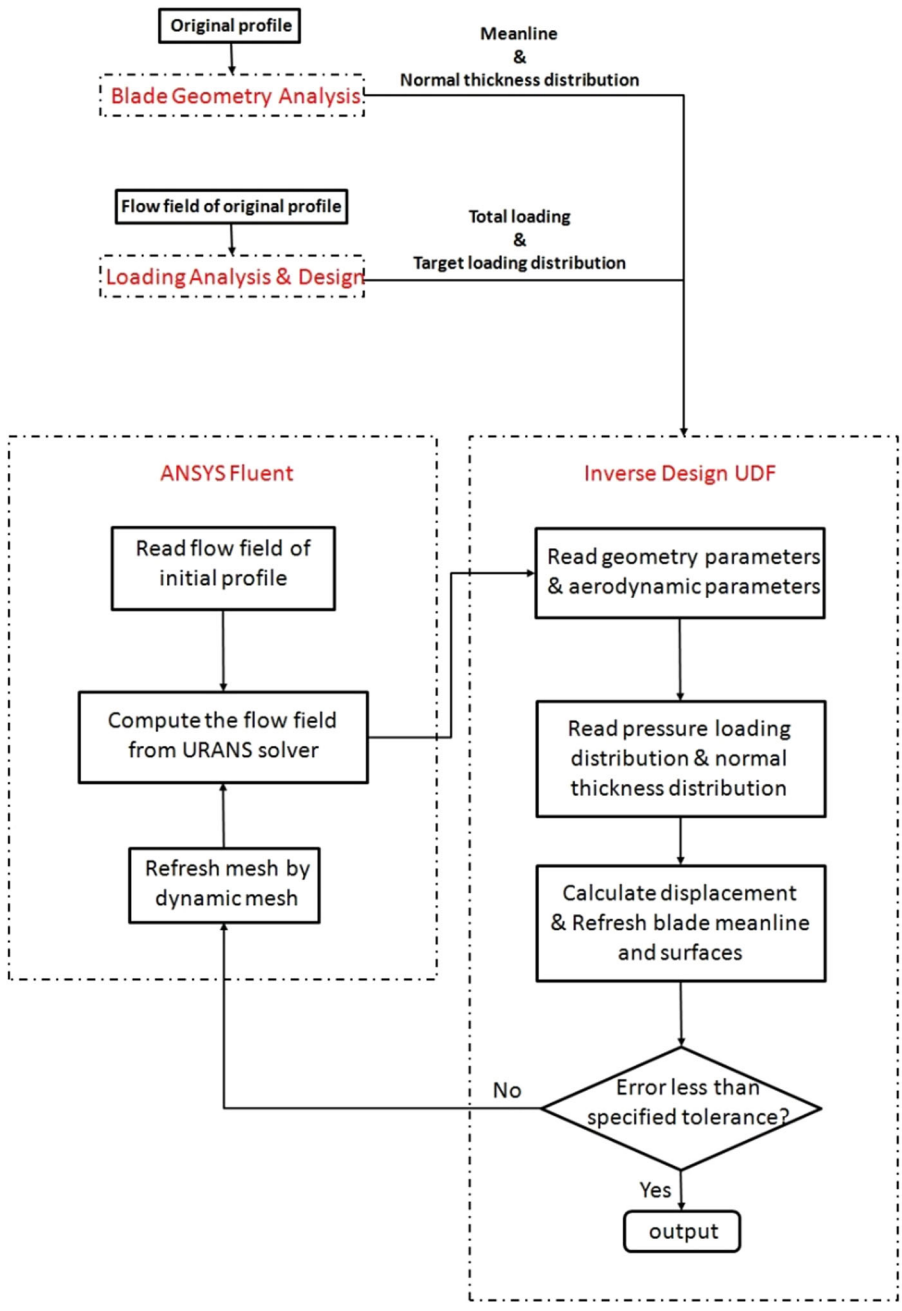

Figure 3. Process of inverse design. UDF = user-defined function.

during the inverse design process. At each modification step, target pressure on the pressure surface and suction surface are updated as follows:

$$p_d = \frac{1}{2}\left(p_{ps}^n + p_{ss}^n\right) \pm \frac{1}{2}\Delta p_d \tag{10}$$

Once the displacements on the pressure surface and suction surface have been solved, the final displacement in the meanline is

$$\Delta_{\text{meanline}} = \frac{1}{2}(\Delta_{ps} + \Delta_{ss}) \tag{11}$$

Because the flow is complicated near the leading edge and trailing edge region, if the inverse design still runs in these regions, the calculation may become unstable. As a result, the inverse design is carried out in the range of 2–98% axial chord position. Blade smoothing is also necessary to guarantee reasonable blade profiles during the inverse design process. Hence, the cubic polynomial based on least squares is employed to fit the blade curves.

3.4. Inverse design process

The core of the inverse design process is the inverse design UDF, which is embedded in ANSYS Fluent. The whole inverse design process is displayed in Figure 3. First, the meanline and normal thickness distribution are extracted from the original blade geometry, which can be imported as initial-guess geometry. Then, the steady flow field of the computational domain constructed from the original blade is imported as the initial condition of the inverse design. At each modification step, the inverse design UDF reads the current flow field from ANSYS Fluent and calculates the displacement on the blade surfaces with the imported geometric parameters and target loading distribution. If the residual meets the required tolerance or changes only a little, then the new blade profile and flow field are exported. Otherwise, the mesh is updated and the flow field is refreshed for the next modification step.

4. Validation of numerical methods

Before presenting any specific inverse design cases, it is necessary to verify the numerical methods be employed in this paper. The compressor cascade V103-220 shown in Figure 4 is chosen as the verification model. It was designed for the hub section of a stator blade in a highly loaded axial compressor (Bell & Fottner, 1995; Hilgenfeld, Cardamone, & Fottner, 2003). This compressor cascade is constructed by conventional NACA-65 blades with a circular camber line. Under the design condition, the inlet Mach number is 0.67 and the inlet Reynolds

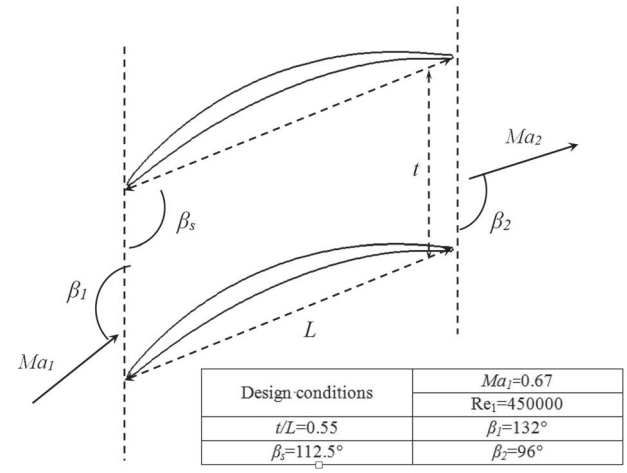

Figure 4. V103-220 compressor cascade.

number based on chord length is 4.5×10^5. This will result in a completely high subsonic flow regime in the flow channel. A supersonic flow region will appear in the flow channel, with a heavy shock boundary-layer interaction on the suction surface when the inlet Mach number increases to a value higher than the critical value of 0.75. Furthermore, the flow along the mid-span of the cascade can be regarded as approximately two-dimensional flow. In view of these facts, the V103-220 compressor cascade is considered to be an appropriate model for investigating inverse design under high subsonic and transonic flow regimes. More detailed information about the test facility and measuring techniques of this compressor cascade can be found in Bell are Fottner (1995) and Hilgenfeld et al. (2003).

The mesh of the computational domain is generated from the ANSYS gambit mesh tool. Figure 5 displays the mesh of the computational domain and the details close to the blade wall. The mesh consists of the boundary layer mesh around the blade surfaces and the unstructured mesh filling the rest of the computational domain. The

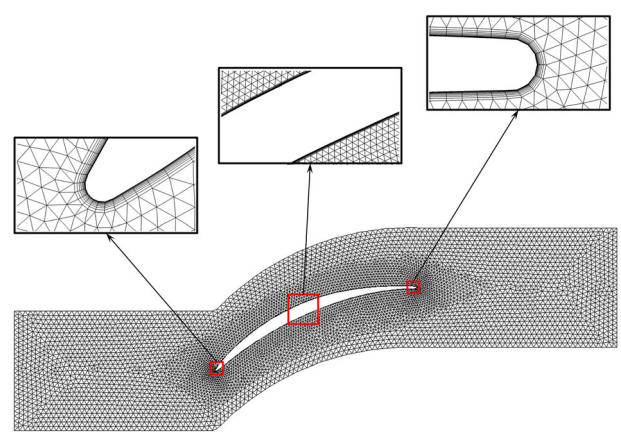

Figure 5. Mesh of the computational domain.

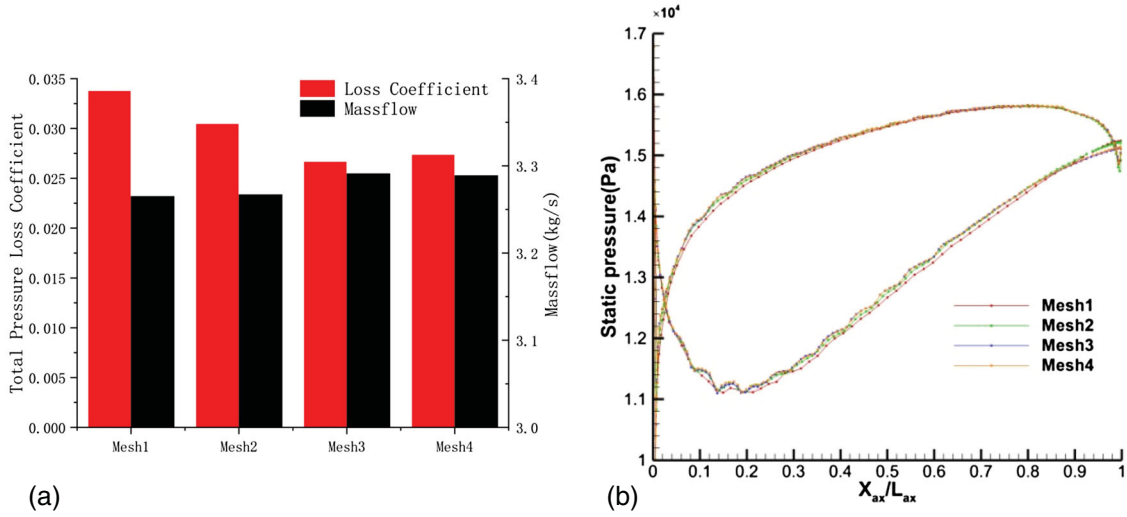

Figure 6. Mesh independence test: (a) loss coefficient and mass flow; (b) static pressure on the blade surfaces.

reason for choosing this hybrid mesh is that unstructured mesh has more robust performance than structured mesh when dealing with boundary deformation (Batina, 1990), and adequate numbers of boundary layers contribute toward resolving the flow near the blade wall.

A mesh independence test was conducted using four mesh levels which correspond to 8×10^3 (Mesh1), 2×10^4 (Mesh2), 5×10^4 (Mesh3) and 1×10^5 (Mesh4) elements. The results displayed in Figure 6 indicate that the finest mesh, Mesh4, hardly helps to improve the predicted result. Thus, Mesh3 is used to discretize the computational domain. Figure 7 shows the y^+ number along the blade surfaces which satisfies the demand of the S-A one-equation turbulence model. The time step is set to be 10^{-4} s in the URANS simulation. The inlet Mach number and Reynolds number are consistent with the experimental requirements by simultaneously adjusting the total pressure, the total temperature at the inlet and the static pressure at the outlet.

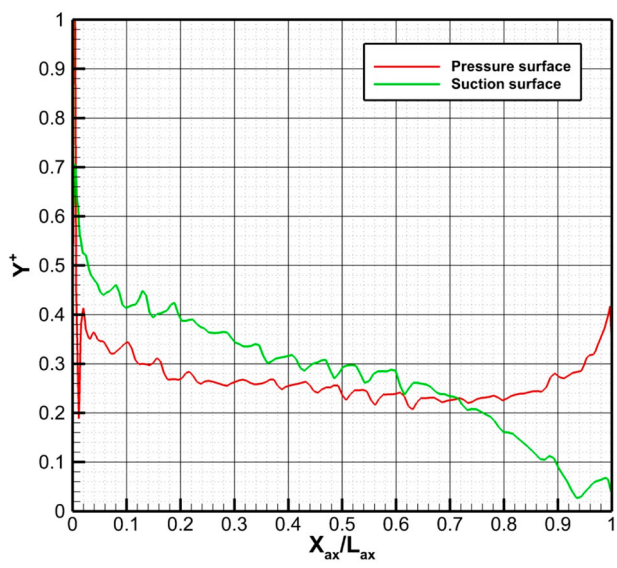

Figure 7. y^+ on the blade surfaces

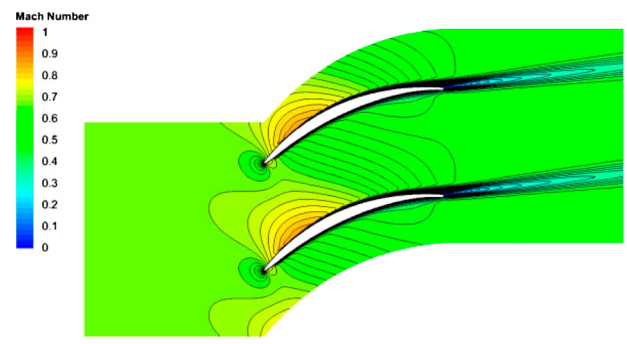

Figure 8. Mach number contour of the original blade (inlet Ma: 0.67).

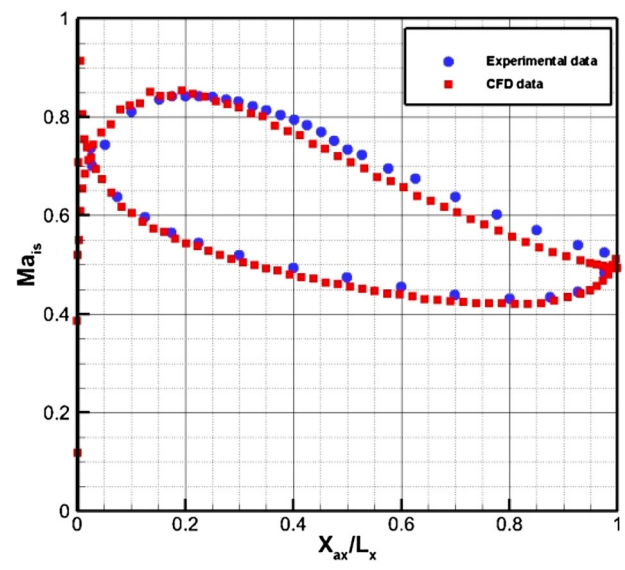

Figure 9. Isentropic Mach numbers of experiment and computational fluid dynamics (CFD) on the blade surfaces.

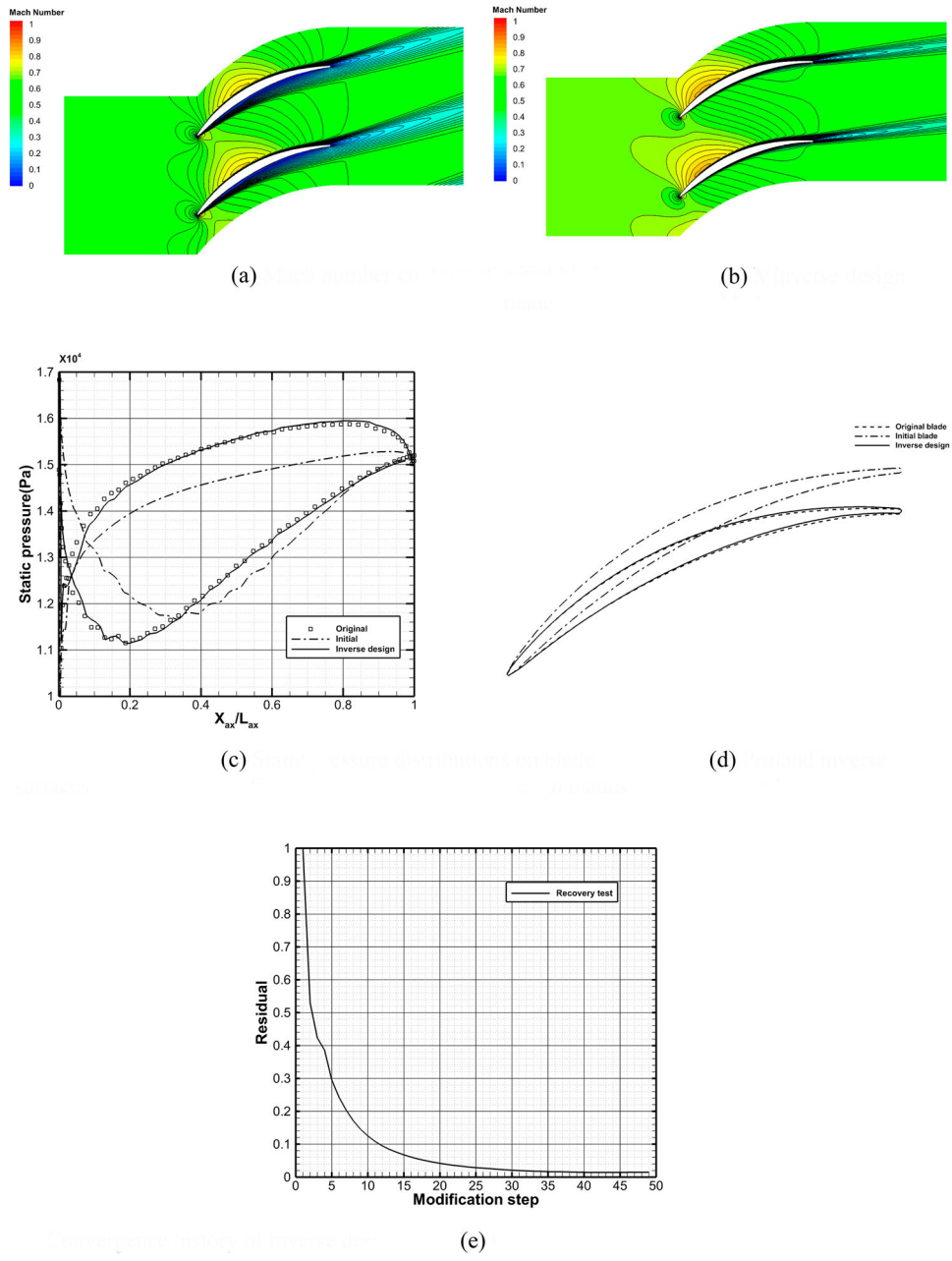

Figure 10. Recovery test of the inverse design method: (a) Mach number contour of initial blade; (b) Mach number contour of inverse design blade; (c) static pressure distributions on blade surfaces; (d) profiles of original, initial and inverse design blades; (e) convergence history of inverse design.

Figure 8 shows the Mach number contour in the original blade passage under the design condition. Figure 9 plots the isentropic Mach number of the CFD simulation and experimental data along the blade surfaces. It can be concluded that the predicted results from CFD are almost consistent with the experimental data. Only a few discrepancies exist on the suction surface, which are caused by a couple of factors. On the one hand, the numerical simulation is completely solved in purely two-dimensional flow, whereas the experimental data were measured in the actual three-dimensional cascade with axial velocity density ratio (AVDR) = 1.0612. On the other hand, a small geometric error between the simulation and the experiment is inevitable. In general, the agreement is considered acceptable for the purpose of this work.

5. Recovery test

In this section, a recovery test is carried out to validate the developed inverse design UDF. The blade geometry of V103-220 is changed intentionally as the initial blade

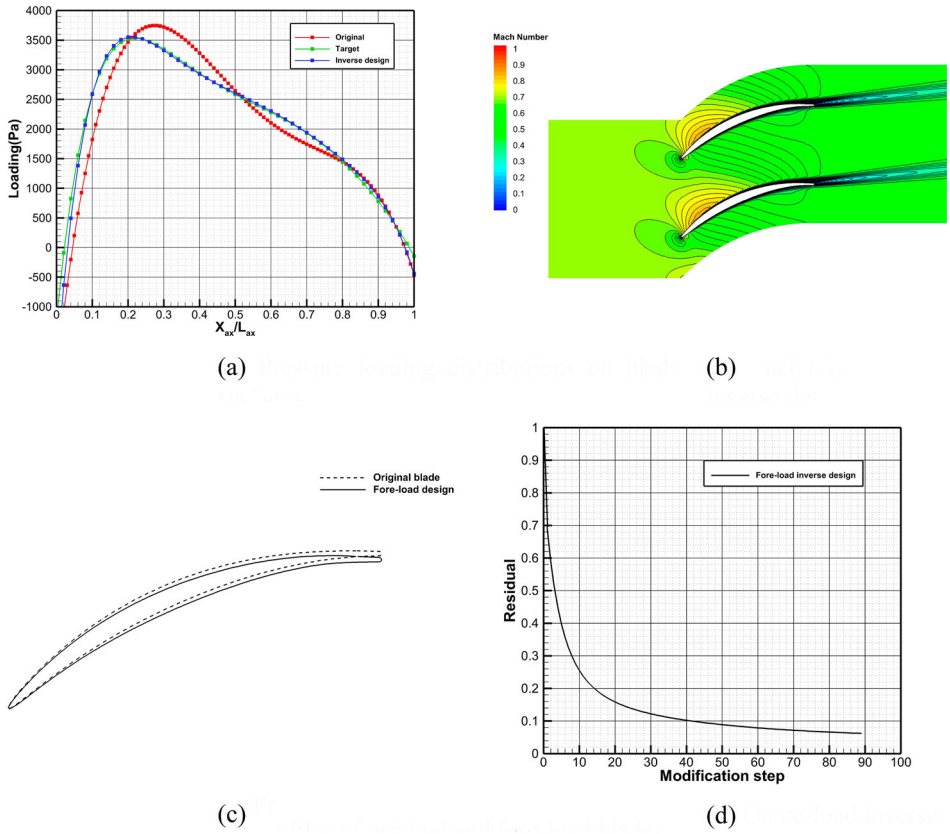

Figure 11. Fore-load inverse design: (a) pressure loading distributions on blade surfaces; (b) Mach number contour of fore-load inverse design; (c) profiles of original and fore-load blades; (d) convergence history of fore-load inverse design.

geometry by modifying the original meanline curve but keeping the original normal thickness distribution unchanged.

Figure 10(a) plots the Mach number contour of the modified blade passage. There are great changes compared with the original flow field shown in Figure 8. The pressure loading distribution along the blade surfaces of the original blade is obtained by running the flow solver in analysis mode. This pressure loading distribution is imposed on the modified blade surfaces as the target pressure loading distribution in the inverse design. If the changed blade geometry can recover to the original blade geometry after the inverse design calculation, this would confirm that this inverse design UDF works successfully.

As shown in Figure 10(b)–(d), there are large differences in flow field and geometry between the original blade and the initial blade. However, the flow field, the static pressure distribution and blade geometries have recovered after 49 modification steps. The convergence history of the inverse design is shown in Figure 10(e). The residual of the inverse design is defined as the mean sum of square of difference between the normalized target and current pressure loading. Given the above results, the feasibility of the inverse design UDF is confirmed.

6. Inverse design cases

6.1. Pressure loading pattern inverse design

In the first inverse design case, three loading distributions are redesigned for V103-220 under its design condition to demonstrate the ability of inverse design UDF to realize the prescribed pressure loading distributions. From the red line in Figure 11(a), which represents the pressure loading distribution along the original blade surfaces, it can be observed that the pressure loading distribution of the original blade is apparently fore-load and the pressure loading peak exists at about the 0.27 axial chord position.

At first, the pressure loading distribution is reorganized but keeps the fore-load pattern. The target loading distribution is depicted in the green line of Figure 11(a). It is shown that the position of the loading peak moves toward the leading edge. The Mach contour of the new fore-load design is displayed in Figure 11(b). The comparison of blade geometries is plotted in Figure 11(c). Figure 11(d) demonstrates that 89 modifications occur in the inverse design process.

In the next case, a mid-load pattern plotted in the green line of Figure 12(a) is expected as the target pressure distribution, where the peak of pressure loading is at the 0.5 axial chord position. After 91 modification steps,

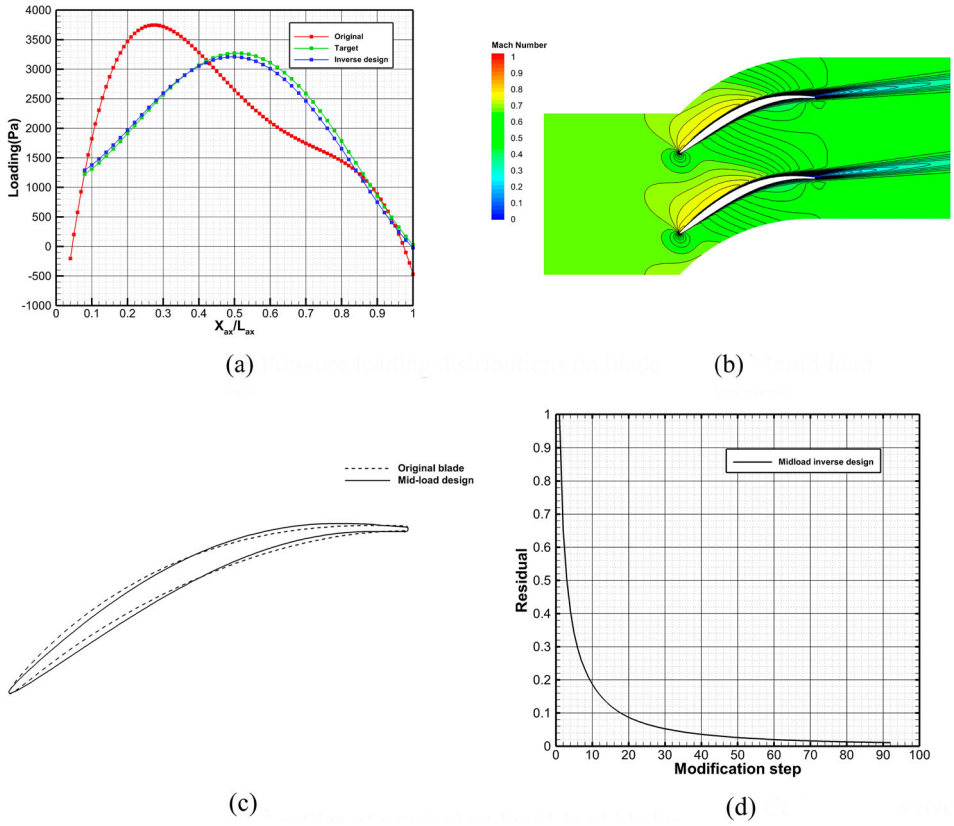

Figure 12. Mid-load inverse design: (a) pressure loading distributions on blade surfaces; (b) Mach number contour of mid-load inverse design; (c) profiles of original and mid-load blades; (d) convergence history of mid-load inverse design.

as observed from the convergence history in Figure 12(d), the residual curve tends to stabilize. At this time, the blade geometry and flow field are almost unchanged. The solution of the inverse design calculation plotted in the blue line is displayed in Figure 12(a). It is concluded that the pressure loading distribution of the inverse design is highly consistent with the target mid-load distribution, although there are a few discrepancies. The flow field of the mid-load inverse design is described in Figure 12(b). Compared with the original blade geometry plotted in the dashed line of Figure 12(c), the blade profile depicted by the solid line is flatter near the leading edge region and more curved near the trailing edge region after the inverse design. Therefore, the intensity of compression is released near the leading edge region but improved close to the trailing edge region.

The third case aims to realize the aft-load using the inverse design UDF. The convergence history plotted in Figure 13(d) shows that the aft-load inverse design process experiences about 130 modification steps when there is little fluctuation in the residual.

The green line of Figure 13(a) displays the target pressure loading distribution of the aft-load, where the load peak appears at the 0.65 axial chord position. The target pressure loading distribution of the aft-load has good agreement with the solution of the inverse design plotted in the blue line. Figure 13(b) plots the flow field of the aft-load inverse design.

In Figure 13(c), the solid line represents the blade geometry of the aft-load inverse design and the dashed line represents the original blade geometry. The features of the aft-load blade geometry exported from the inverse design calculation are that the curvature becomes flatter in the leading edge region and is more curved in the trailing edge region in comparison with the original and mid-load blades. This means the compression process of gas is further strengthened near the trailing edge region and is released near the leading edge region. The design of the pressure loading distribution, changing from fore-load to mid-load and aft-load design, has demonstrated that the developed inverse design method has good performance in realizing the prescribed pressure loading distribution.

All of the cases presented above were executed in a serial process on a personal computer with an Intel i7-7700 processor. The computational information and total pressure loss coefficients of these three designs are included in Table 1. It is clear that the

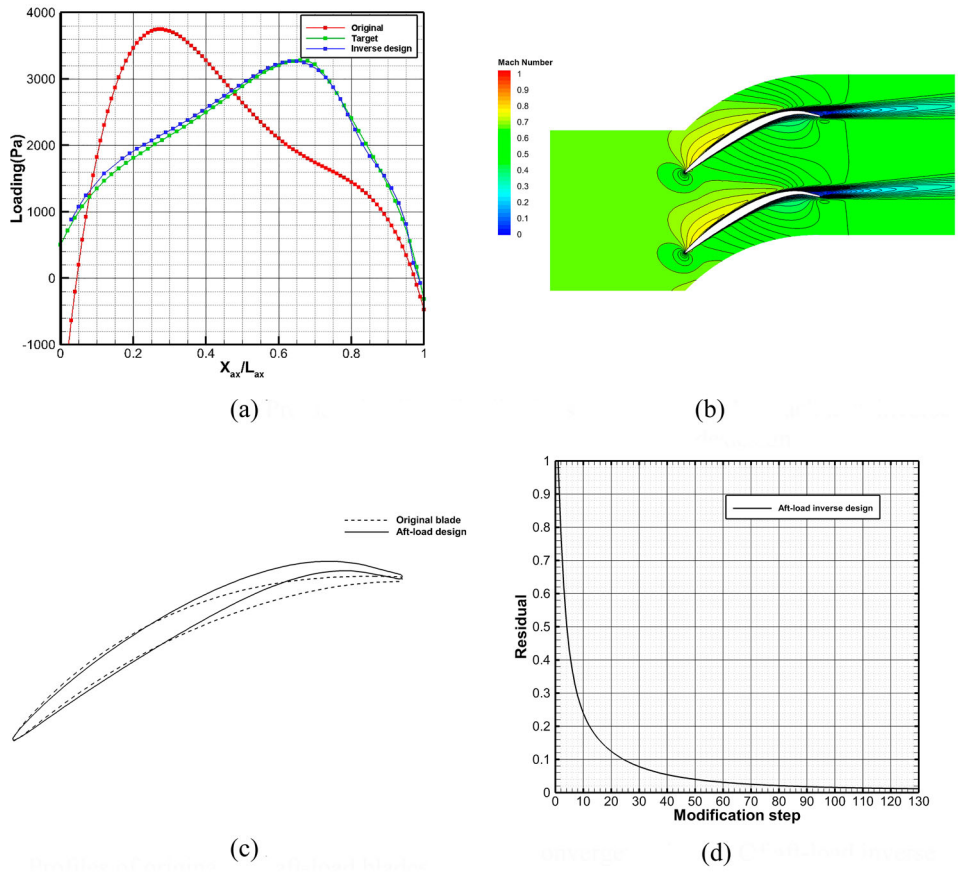

Figure 13. Aft-load inverse design: (a) pressure loading distributions; (b) Mach number contour of aft-load inverse design; (c) profiles of original and aft-load blades; (d) convergence history of aft-load inverse design.

Table 1. Total pressure loss and computational information of different loading designs.

Case	Total pressure loss coefficient	Time	Resources
Base	0.0267	–	PC CPU: Intel i7-7700 3.60 GHz
Fore-load	0.0258	2 h	
Mid-load	0.0300	2 h	
Aft-load	0.0400	2.7 h	

new fore-load design could decrease the total pressure loss.

6.2. Pressure loading smooth inverse design

The cases described in Subsection 6.1 are for absolutely subsonic flow regimes in the flow passage with the inlet Mach number 0.67. When the inlet Mach number increases to a value higher than 0.75, a shock wave will appear in the flow passage. Therefore, the effect of the inverse design method will be investigated under transonic flow in this case.

The inlet Mach number is increased from 0.67 to 0.8. Different turbulence models, such as the S-A, k-ϵ and k-ω models, are used to research the sensitivity of the inverse design solution because of the existence of shock waves. Figure 14 depicts the y^+ with different turbulence models. Figure 15 displays the Mach number contour in the flow domain using different turbulence models. There is no doubt that a shock wave covers the flow channel and impacts on the suction surface. Because of the existence of the shock wave, the pressure loading along the blade surfaces will appear to be discontinuous.

Figure 16 compares the isentropic Mach number distribution on the pressure and suction surface between the experimental data and the CFD solution with different turbulence models. It seems that the k-ϵ model predicts a stronger shock wave. Although there are some discrepancies, the trend predicted by CFD is consistent with the experimental results.

Total pressure loss will be caused when the flow moves across a shock wave. In addition, the interaction of the shock wave and boundary layer may increase the risk of flow separation. Hence, the principle of this case is smoothing the pressure loading distribution along the blade surfaces to decrease both the total pressure loss and the risk of flow separation caused by the shock wave. At the same time, the total

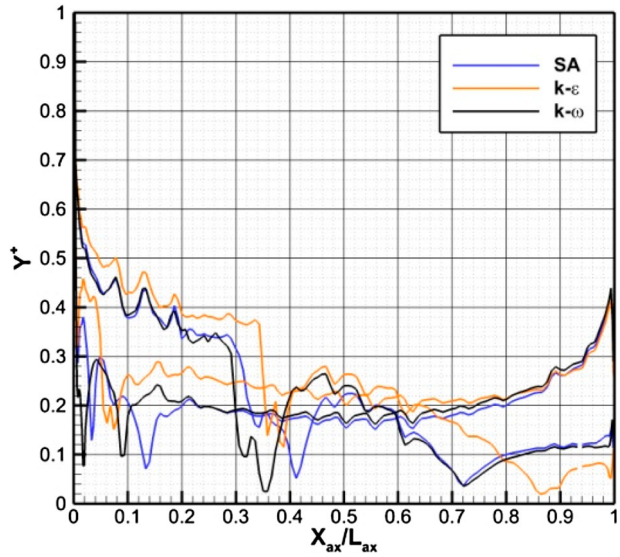

Figure 14. y^+ on the blade surfaces for different turbulence models. SA = Spalart–Allmaras.

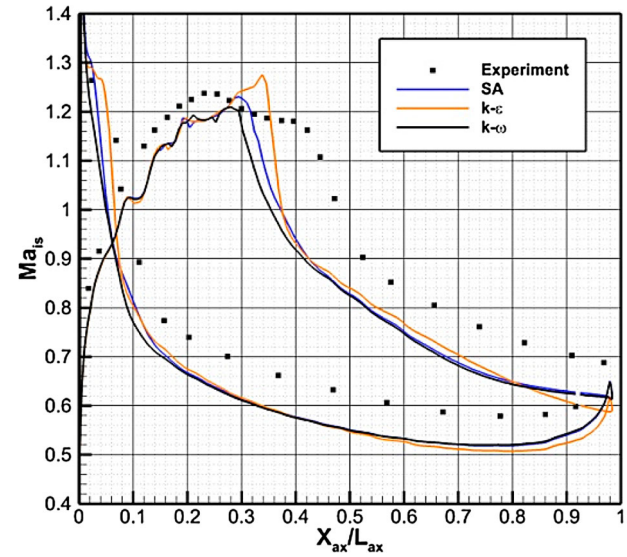

Figure 16. Isentropic Mach numbers of experiment and computational fluid dynamics (CFD) on the blade surfaces for different turbulence models. SA = Spalart–Allmaras.

pressure loading is kept unchanged to guarantee the pressure ratio when designing the target pressure loading distribution.

It can be observed from the green line of Figure 17(a) that the peak of target loading decreases from the original 6300 Pa to 4700 Pa. The decreased pressure loading is compensated in other regions to maintain the total pressure loading. In general, the pressure loading distributions calculated from the inverse design using different turbulence models are consistent with the prescribed pressure loading distribution shown in Figure 17(a). However, there exists a defect with the use of the k-ϵ model.

Figure 17(b)–(d) displays the flow field after the smooth inverse design with different turbulence models. The changes in blade geometry after the inverse design can be observed in Figure 17(e). This shows that the blade geometry obtained from using the k-ϵ turbulence model has some different features near the trailing edge. The blade profile obtained from the smooth inverse design has the feature that the curvature close to the leading

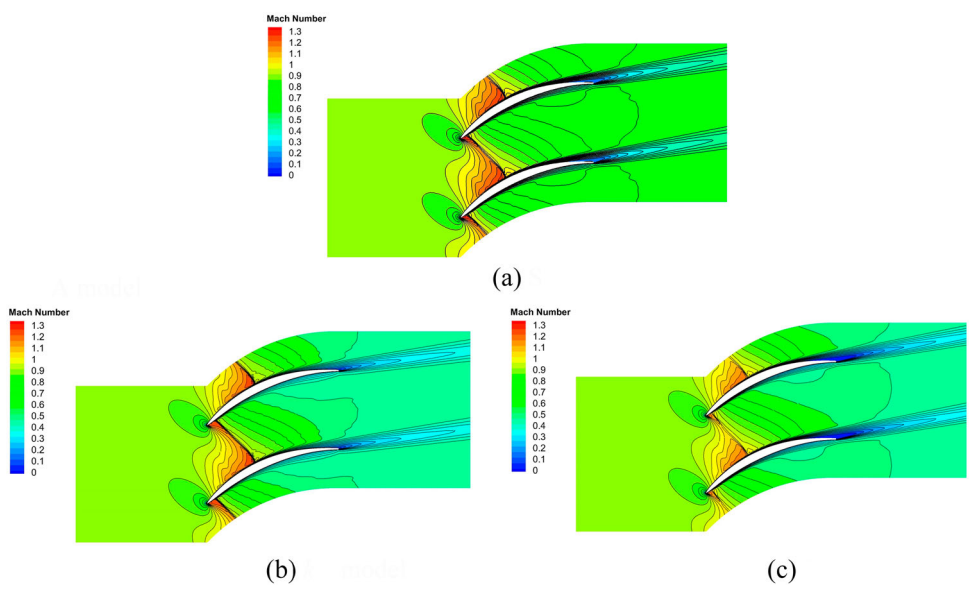

Figure 15. Mach number contour of original blade passage with different turbulence models (inlet Ma: 0.8): (a) Spalart–Allmaras (S-A) model; (b) k-ϵ model; (c) k-ω model.

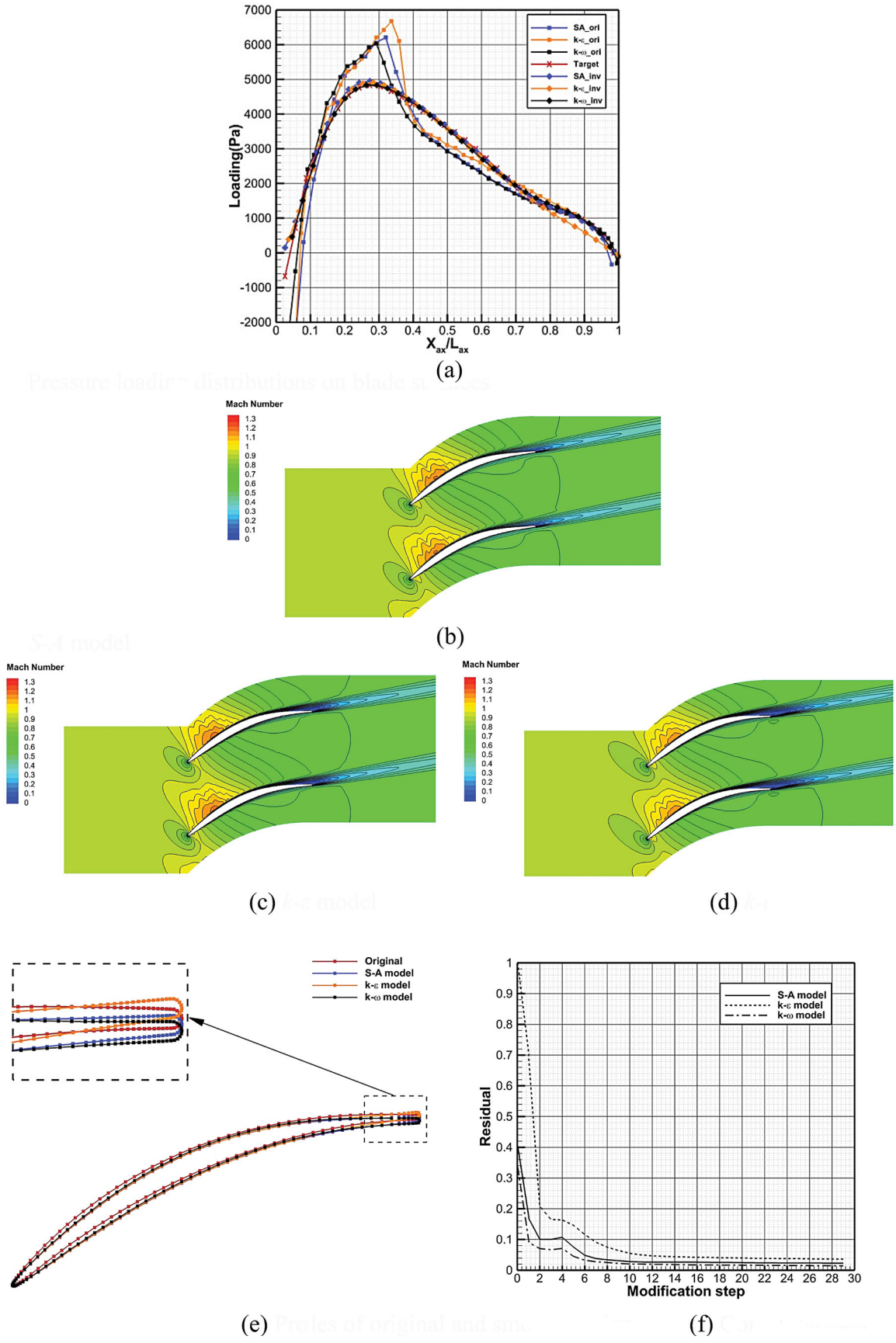

Figure 17. Smooth inverse design: (a) pressure loading distributions on blade surfaces; (b) Spalart–Allmaras (S-A) model; (c) k-ϵ model; (d) k-ω model; (e) profiles of original and smooth design blades; (f) convergence history of smooth inverse design.

Table 2. Total pressure loss and computational information of smooth loading designs.

Case	Total pressure loss coefficient	Time	Resources
Base	0.0539	–	PCCPU: Intel i7-7700 3.60 GHz
Spalart–Allmaras model	0.0359	40 min	
k-ϵ model	0.0334	40 min	
k-ω model	0.0367	40 min	

edge decreases a little, but increases slightly approaching the trailing edge compared with the original blade geometry. Although there are a few changes in the blade geometry after the smooth inverse design under the transonic flow regime, the flow field changes obviously with the control of the flow acceleration on the blade surfaces. In the changed flow field, the pressure loading on the blade surfaces becomes smooth and the shock wave disappears. Hence, the shock boundary-layer interaction is eliminated and the total pressure loss caused by the shock wave is decreased. The convergence history depicted in Figure 17(f) demonstrates that the result found with the k-ω model has superior accuracy. The computational information and total pressure loss are included in Table 2.

7. Conclusion

The viscous inverse design is implemented by embedding the UDF with the N-S solver and dynamic mesh, which saves the time spent on remeshing the computational domain. A variable relaxation factor is introduced to control the deformation size for different cases in this paper. The recovery test proves the success of the inverse design UDF. In addition, a case of different patterns of pressure loading distribution in a high subsonic flow regime demonstrates the ability of the developed inverse design UDF to manage the pressure loading distribution on the blade surfaces. The fore-load, mid-load and aft-load patterns are realized using this inverse design UDF. The results indicate that the new fore-load design can decrease the total pressure loss. With a higher inlet Mach number, a case of smooth loading design proves that this inverse design UDF can deal with the loading design in transonic flow. Using the smooth inverse design, the shock wave is removed. As a result, the total pressure loss decreases and the pressure loading on the blade surfaces is smoothed.

In future research, this two-dimensional inverse design method will be extended to three-dimensional flow for engineering practice. Besides, the strategies of the prescribed pressure loading distribution on the blade surfaces will be explored and summarized to realize higher efficiency and a broader working range. Attention will also be paid to how to use the inverse design to implement different aerodynamic design objectives.

Disclosure statement

No potential conflict of interest was reported by the authors.

Funding

This work was supported by National Science and Technology Major Project [grant number 2017-II-0006-0019].

References

Arbabi, A., & Ghaly, W. (2013). Inverse design of turbine and compressor stages using a commercial CFD program. In *ASME. Turbo Expo: Power for land, sea, and air, Volume 6B: Turbomachinery*. San Antonio, USA.

Arbabi, A., Ghaly, W., & Medd, A. (2017). Aerodynamic inverse blade design of axial compressors in three-dimensional flow using a commercial CFD program. In *ASME. Turbo Expo: Power for land, sea, and air, Volume 2B: Turbomachinery*. Charlotte, USA.

Batina, J. T. (1990). Unsteady Euler airfoil solutions using unstructured dynamic meshes. *AIAA Journal*, *28*(8), 1381–1388.

Bell, R. M., & Fottner, L. (1995). Investigations of shock/boundary-layer interaction in a highly loaded compressor cascade. In *ASME. Turbo Expo: Power for land, sea, and air, Volume 1: Turbomachinery*. Houston, USA.

Borges, J. E. (1990). A three-dimensional inverse method for turbomachinery: Part I—theory. *Journal of Turbomachinery*, *112*(3), 346–354.

Daneshkhah, K., & Ghaly, W. (2007). Aerodynamic inverse design for viscous flow in turbomachinery blading. *Journal of Propulsion and Power*, *23*(4), 814–820.

Dang, T., Damle, S., & Qiu, X. (2000). Euler-based inverse method for turbomachine blades, part 2: Three-dimensional flows. *AIAA Journal*, *38*(11), 2007–2013.

Dang, T., & Isgro, V. (1995). Euler-based inverse method for turbomachine blades. I—Two-dimensional cascades. *AIAA Journal*, *33*, 2309–2315.

Demeulenaere, A., Léonard, O., & Van den Braembussche, R. (1997). A two-dimensional Navier-Stokes inverse solver for compressor and turbine blade design. *Proceedings of the Institution of Mechanical Engineers, Part A: Journal of Power and Energy*, *211*(4), 299–307.

Demeulenaere, A., & Van den Braembussche, R. (1998). Three-dimensional inverse method for turbomachinery blading design. *Journal of Turbomachinery*, *120*(2), 247.

De Vito, L., Van den Braembussche, R. A., & Deconinck, H. (2002). A novel two dimensional viscous inverse design method for turbomachinery blading. In *ASME Turbo Expo 2002: Power for land, sea, and air, Volume 5: Turbo Expo 2002, Parts A and B*. Amsterdam, Netherlands.

Eivaz, A., Bahman, N., Mohsen, J., Sina, F. A., Shahaboddin, S., & Chau, K. W. (2018). Experimental and computational fluid dynamics-based numerical simulation of using natural gas in a dual-fueled diesel engine. *Engineering Applications of Computational Fluid Mechanics*, *12*(1), 517–534.

Ferlauto, M., & Marsilio, R. (2006). A viscous inverse method for aerodynamic design. *Computers & Fluids*, *35*(3), 304–325.

Ghalandari, M., Mirzadeh Koohshahi, E., Mohamadian, F., Shamshirband, S., & Chau, K. W. (2019). Numerical simulation of nanofluid flow inside a root canal. *Engineering Applications of Computational Fluid Mechanics*, *13*(1), 254–264.

Hilgenfeld, L., Cardamone, P., & Fottner, L. (2003). Boundary layer investigations on a highly loaded transonic compressor cascade with shock/laminar boundary layer interactions. Proceedings of the Institution of Mechanical Engineers, Part A. *Proceedings of the Institution of Mechanical Engineers, Part A: Journal of Power and Energy*, *217*(4), 349–356.

Lighthill, M. J. (1945). A new method of two-dimensional aerodynamic design. *Aeronautical Research Council R&M*.

Madadi, A., Kermani, M. J., & Nili, M. (2015). Three-dimensional design of axial flow compressor blades using the ball-spine algorithm. *Journal of Applied Fluid Mechanics*, *8*(4), 683–691.

Mileshin, V. I., Orekhov, I. K., Shchipin, S. K., & Startsev, A. N. (2004). New 3D inverse Navier-Stokes based method used to design turbomachinery blade rows. In *Proceedings of the ASME 2004 heat transfer/fluids engineering summer conference. Volume 2, Parts A and B* (pp. 881–889). Charlotte.

Mosavi, A., Shamshirband, S., Salwana, E., Chau, K. W., & Tah, J. H. M. (2019). Prediction of multi-inputs bubble column reactor using a novel hybrid model of computational fluid dynamics and machine learning. *Engineering Applications of Computational Fluid Mechanics*, *13*(1), 482–492.

Roidl, B., & Ghaly, W. (2010). Redesign of a low speed turbine stage using a new viscous inverse design method. *Journal of Turbomachinery*, *133*(1), 011009-9.

Sanz, J. M. (1988). Automated design of controlled-diffusion blades. *Journal of Turbomachinery*, *110*(4), 540–544.

Thompkins, W. T., & Tong, S. (1982). Inverse or design calculations for nonpotential flow in turbomachinery blade passages. *Journal of Power and Energy*, *104*(2), 281–285.

Van Rooij, M., & Medd, A. (2012). Reformulation of a three-dimensional inverse design method for application in a high-fidelity CFD environment. In *Proceedings of the ASME Turbo Expo 2012: Turbine technical conference and exposition. Volume 8: Turbomachinery, Parts A, B, and C* (pp. 2395–2403). Copenhagen.

Yang, J., Liu, Y., Wang, X., & Wu, H. (2017). An improved steady inverse method for turbomachinery aerodynamic design. *Inverse Problems in Science and Engineering*, *25*(5), 633–651.

Zannetti, L., & Pandolfi, M. (1984). Inverse design technique for cascades. NASA-CR-3836.